ACS APPLIED MATERIALS & INTERFACES

www.acsami.org

Research Article

Hierarchically Porous Ceramics via Direct Writing of Binary Colloidal Gel Foams

Benito Román-Manso, Joseph Muth, Lorna J. Gibson, Wolfgang Ruettinger, and Jennifer A. Lewis*

Cite This: https://dx.doi.org/10.1021/acsami.0c22292

Read Online

ACCESS | Metrics & More | Article Recommendations | Supporting Information

ABSTRACT: Hierarchically porous ceramics with a high specific surface area and interconnected porosity may find potential application as particulate filters, catalyst supports, and battery electrodes. We report the design and programmable assembly of cellular ceramic architectures with controlled pore size, volume, and interconnectivity across multiple length scales via direct foam writing. Specifically, binary colloidal gel foams are created that contain entrained bubbles stabilized by the irreversible adsorption of attractive alumina and carbon (porogen) particles at their air−water interfaces. Composition effects on foam ink rheology and printing behavior are investigated. Sintered ceramic foams exhibited specific permeabilities that increased from 2×10^{-13} to 1×10^{-12} m^2 and compressive strengths that decreased from 40 to 1 MPa, respectively, with increasing specific interfacial area. Using direct foam writing, 3D ceramic lattices composed of open-cell foam struts were fabricated with tailored mechanical properties and interconnected porosity across multiple length scales.

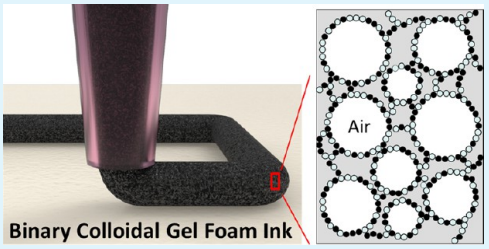

KEYWORDS: *3D printing, particle-stabilized foams, cellular ceramics, hierarchical porosity, particle filtration*

1. INTRODUCTION

Hierarchical cellular structures are ubiquitous in nature due to their mechanical efficiency and multifunctionality.[1−7] Inspired by natural systems, synthetic materials have been produced by bulk casting[8−10] and additive manufacturing[11−13] methods. Specifically, open- and closed-cell foams have been fabricated by casting particulate suspensions that contain pore-forming agents (porogens)[8,14] as well as particle-stabilized foams.[9,10,15] While ceramic foams can be readily generated, they are limited to simple 3D shapes that possess a bending-dominated mechanical response.[13,16] Emerging efforts have focused on fabricating multiscale metamaterials via light-based 3D printing of photopolymerizable organic[11,12,17−20] and preceramic resins.[21] To date, 3D microlattices, octet trusses, and tetrakaidecahedra with struts composed of hollow shells,[11,12,17,19] solid features,[20,21] or even finer trusses[17,18] have been produced that exhibit bending, stretching, or mixed-mode mechanical responses.

We recently introduced a new method for fabricating closed-cell ceramic foams and 3D periodic lattices, known as direct foam writing.[13,16] Colloidal gel foam inks were developed that contained entrained bubbles stabilized by attractive colloidal particles, which irreversibly adsorb onto their liquid−air interfaces. These attractive colloidal particles also form a spanning network (or gel) in suspension. The printed 3D ceramic lattices exhibited high specific stiffness values that were superior to bulk foams and microlattices of similar total porosity produced via light-based 3D printing. However, their closed-cell struts lacked interconnected porosity needed for many applications of interest, including particle filtration,[22] catalyst supports,[23] and battery electrodes.[24−26]

To promote efficient fluid transport, one must create porous materials with tailored pore volume, size, and interconnectivity. Under high-velocity conditions, the pressure drop (ΔP) across a given porous material is well described by eq 1, which combines Darcy's law with Forchheimer's extension

$$\frac{\Delta P}{L} = \frac{\eta}{k} v + \beta \rho v^2 \tag{1}$$

where L is the sample thickness, v is the fluid velocity, η is the dynamic viscosity of the fluid, ρ is the fluid density, k is the specific permeability, and β is the inertial resistance. When the fluid velocity is low, eq 1 reduces to Darcy's law. The characteristic pore diameter (D) and total porosity, defined by the pore fraction (ε), control the specific permeability (k)

$$k = \frac{\varepsilon^3}{150(1-\varepsilon^2)} D^2 \tag{2}$$

Received: December 16, 2020
Accepted: January 28, 2021

As a benchmark, the reported permeability of porous ceramics used in wall-flow diesel particulate filters, where $D_{wall} \sim 10$ μm and $\varepsilon_{wall} \sim 0.4-0.5$, ranges between $k \sim 10^{-13}$ and 10^{-12} m^2.[27]

Here, we report the design and programmable assembly of hierarchically porous ceramics via direct writing of binary colloidal gel foams. We created foam-based inks composed of a mixture of hydrophobically modified alumina and carbon (porogen) particles that irreversibly adsorb onto liquid−air (bubble) interfaces.[8,13,15,28,29] We then investigated the foam ink rheology and printing behavior. Next, we produced hierarchically porous ceramics by both bulk casting and direct foam writing. Upon sintering, the resulting hierarchically porous ceramics contain open walls (microscale pores), arising from the removal of porogen particles, that surround open cells (mesoscale pores) generated by entrained bubbles. Unlike the cast structures, the printed and sintered 3D ceramic lattices contained a third level of hierarchy resulting from the interconnected pathways (macroscale pores) between patterned features. Finally, we assessed their microstructural evolution, permeability, and compressive mechanical properties to elucidate the effects of hierarchical porosity on their performance.

2. EXPERIMENTAL SECTION

2.1. Binary Colloidal Gel Foams. Binary colloidal gels and foam-based inks are produced by first dispersing an appropriate amount of α-alumina particles (AKP 30 Sumitomo Chemical) with a mean particle size, D, of 300 nm and a specific surface area of ~ 7.5 m^2/g in deionized (DI) water at a pH > 10 (adjusted by adding sodium hydroxide, NaOH). The resulting alumina (stock) suspension is ball milled for 1 week using alumina milling media. Next, carbon black (porogen) particles (Thermax N990, Cancarb LTD; d_{50} = 280 nm and Brunauer−Emmett−Teller surface area ~ 9.4 m^2/g) are added in a step-wise fashion to the stock suspension. The suspension is then mixed for 2 min at 2200 rpm in a planetary mixer (SpeedMixer DAC 600.2; FlackTek, Inc.) after each step-wise carbon black addition. The resulting alumina/porogen particle ratio is 30:70 by volume, which ensures a high degree of porosity without compromising mechanical robustness. Next, an amine surfactant (decylamine, 95%; Sigma-Aldrich) is added to partially hydrophobize both particle populations. The specific concentration (Λ) is varied between 0.3 and 1.2 μmol of decylamine per m^2 of the total particle surface area. The surface tension of each corresponding supernatant solution is measured using the pendant-drop method (Kruss DSA100 Goniometer). The drop geometry is imaged at a rate of 10 frames/s, while its volume is increased at a rate of 10 μL/min^{-1}. To prevent cracking during drying of the cast and 3D printed foams, we incorporated 1 wt % of poly(ethylene glycol) (PEG, M_n ~ 20,000; Sigma-Aldrich) and 1 wt % sucrose as binders. Each suspension is diluted to a total colloid volume fraction between $0.11 < \phi_c < 0.18$ prior to homogenization in a planetary mixer.

Binary colloidal gels are created by adjusting the pH to a value of 10.25 to induce attractive interactions between both particle populations. These precursor gels are transformed into the desired foam-based inks by mechanical frothing using a four-bladed impeller (316L Cross Stirrer; Scilogex) attached to an overhead mixer (OS20-S; Scilogex), which entrains air in the form of bubbles. During mechanical frothing, the inks are mixed at a given speed for 300 s, which is increased from 600 to 1800 rpm in increments of 300 rpm. The mixing intensity levels are denoted by 50% (900 rpm), 70% (1300 rpm), 85% (1500 rpm), and 100% (1800 rpm). Each foam-based ink is subjected to the same protocol up to the stated mixing intensity level.

2.2. Rheological Measurements. Stress viscometry and oscillatory measurements are carried out on the binary colloidal gels and foams at 21 °C using a hybrid rheometer (Discovery HR-3 hybrid rheometer; TA Instruments) equipped with a custom-made 8-bladed vane (15 mm diameter, 38.5 mm height, 1.3 mm blade thickness, 4 mm gap) and a solvent trap to prevent evaporation. The foams are loaded into the cup immediately after frothing. Prior to the measurements, foams are equilibrated under a low-amplitude oscillatory strain (γ = 0.001) until G' remains approximately constant (typically 15−30 min). After equilibration, stress sweeps are carried out between 0.01 and 250 s^{-1}. Their shear yield stress (τ_y) is defined by the crossover point, where G'' exceeds G'.

2.3. Foam Casting and Printing. Bulk foams are created by casting foam-based inks into rectangular plastic molds (60 × 25 × 10 mm), which are precoated with a thin layer of petroleum jelly to facilitate removal. During the casting process, each mold is manually shaken to ensure proper filling and any excess foam is removed using a doctor blade to produce bulk foams with flat (top) surfaces. 3D ceramic lattices are produced by the direct writing of foam-based inks. Specifically, each foam ink is loaded into a 60 mL syringe and dispensed through a tapered nozzle (Nordson EFD) with varying inner diameter using a syringe pump (PHD Ultra; Harvard Apparatus). Most 3D lattices are printed using a nozzle with a 610 μm inner diameter. The printhead is attached to a custom-built 3D printer (ABG 10000; Aerotech Inc.), whose $x-y-z$ motion is controlled by a customized G-code. Square lattice structures are printed at 37 mm/s with a flow rate of 2.1 mL/min into 18 × 18 × 12 mm shapes utilizing wax-coated (Pure Petroleum Jelly; Vaseline) zirconia plates (Zircoa) as substrates for the ink deposition.

Both cast and printed foam structures are slowly dried under controlled humidity conditions for several days. After drying at room temperature, they are removed from the substrates and heated at 90 °C for 4 h to remove any residual water from the samples. The samples are then heated to 700 °C at 2 °C/min for 3 h to remove the carbon (porogen) particles, followed by heating to 1500 °C at 2 °C/min, where they are held for 2 h, to sinter the alumina particles prior to cooling to ambient temperature.

2.4. Microstructural Evolution. The microstructural evolution of cast and printed foams is characterized using field-emission scanning electron microscopy (Ultra55 Zeiss) after both drying and sintering. Image analysis is carried out to determine the average bubble diameter (d) and average bubble volume fraction (ϕ_b) for each foam sample. Note that the bubbles represent the dispersed phase, while the alumina/porogen particle matrix (or, after sintering, pure alumina) serves as the continuous phase within these foams. The specific bubble surface area (Σ, mm^2/mm^3 or mm^{-1}), which is reported per unit volume of foam, is calculated by $\Sigma = [(6\phi_b)/d] \times 1000$, where ϕ_b and d (μm) are measured experimentally.[16] d is obtained using the linear intercept method for two-phase materials (ASTM E112-13), in which at least 40 mm of lines are analyzed over 5 mm^2. ϕ_b is obtained using the systematic point count method (ASTM E562-08),[16] in which at least 400 grid points are analyzed over 5 mm^2 for each dried foam sample. The reported averages and standard deviations correspond to values obtained from at least three different images.

2.5. Porosity, Permeability, and Particle Filtration Measurements. The porosity of sintered ceramic foams is characterized using mercury intrusion porosimetry (Micromeritics AutoPore). Prior to testing, the samples are heated to 350 °C for 1 h and then cooled to room temperature. The samples are analyzed using a fixed pressure table, which ranges from 1.5 to 60,000 psi, with a 10 s equilibration at each pressure. A blank is run and subtracted from the data. The data are analyzed using the Washburn equation, $D = -(4\gamma \cos q)/P$, where γ is the surface tension of mercury (γ = 0.48 N/m), q is the advancing and receding contact angle (q = 140°), D is the pore diameter, and P is the pressure. The relative density (ρ_{rel}) of each sample is calculated based on the total volume of mercury intruded, where $\rho_{rel} = \rho/\rho_{th} \times 100\%$ and ρ_{th} is the theoretical density of alumina (ρ_{th} = 3.97 g/cm^3).

The permeability, k, of the sintered ceramic foams is measured by flowing air at a rate (Q) of 0.5−1 L/min through disc-shaped samples (thickness, L, of ~1 mm) and a cross-sectional area (A) of ~960 mm^2 and measuring the pressure drop ($\Delta P = p_b - p_a$) using

https://dx.doi.org/10.1021/acsami.0c22292
ACS Appl. Mater. Interfaces XXXX, XXX, XXX−XXX

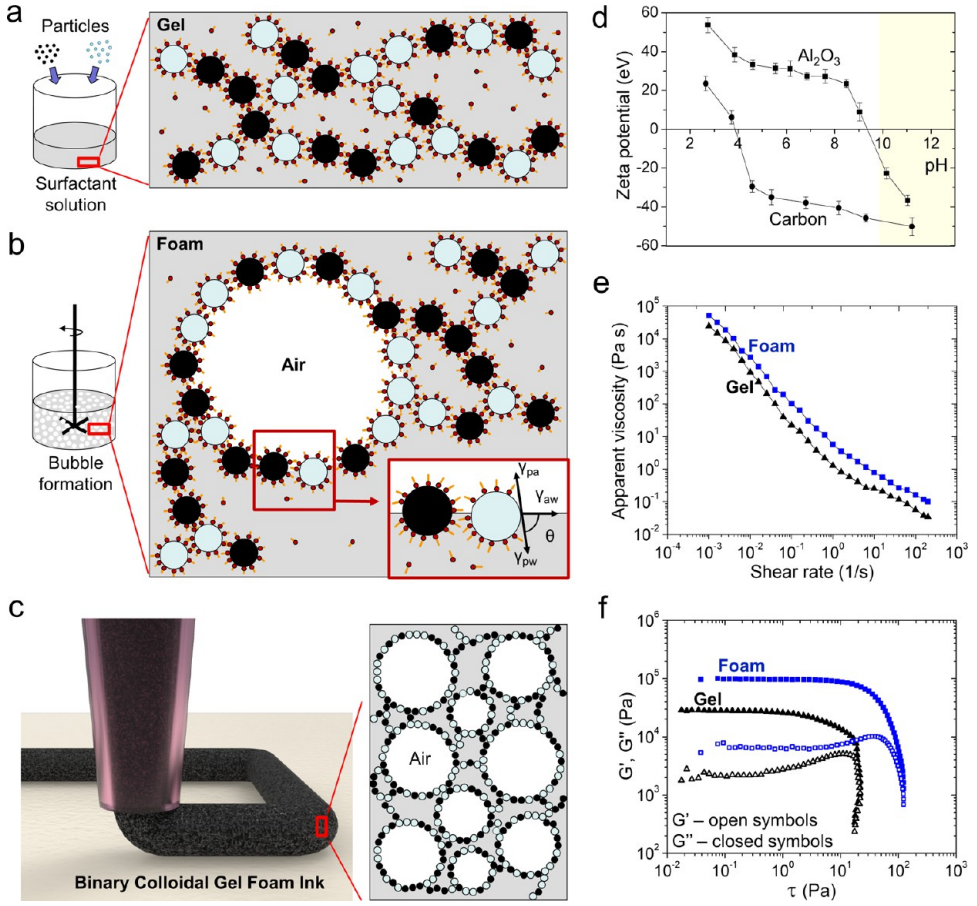

Figure 1. Binary colloidal gel foams. (a) In aqueous-based binary gels, both alumina and carbon (porogen) particles are similarly hydrophobized with amphiphilic surfactant molecules in a single step. (b) After the incorporation of air by mechanical frothing, both types of particles are driven to the bubble/water interfaces. In the inset, the irreversible adsorption of the particles to the interfaces is quantified by a contact angle of around 90°, with partial wetting from both fluid phases. (c) Schematic view of direct writing of binary colloidal gel foams into filaments. (d) Zeta potential vs pH plot for both particle populations. (e,f) Plots of apparent viscosity as a function of shear rate and storage (G') and loss moduli (G'') as a function of shear stress (τ) for a representative binary colloidal gel before and after mechanically mixing to create a foam ink.

pressure transducers. k is given by Darcy's law, $Q = -\frac{kA(p_b - p_a)}{\mu L}$, where μ is the dynamic viscosity of air, and p_b and p_a are the gas pressure measured on each side of the foam disc.

To assess their particle filtration capability, we first prepared an aqueous suspension by mixing 1 μm-sized fluorescent polystyrene beads (PS, FluoSpheres Carboxylate-Modified Microspheres, 1.0 μm, crimson fluorescent (625/645), 2 wt % solids; Thermo Fisher Scientific) with DI water to yield a dilute PS suspension (3×10^{-4} wt % solids). We then flowed 500 ml of this dilute PS suspension through a sintered Al_2O_3 foam (14% of theoretical density) cast in the form of a disc (20 mm in diameter, 3 mm in thickness). After filtration, the foam discs are imaged using a laser scanning confocal microscope (Zeiss LSM 710) to determine the location of the fluorescent PS particles.

2.6. Mechanical Property Measurements. Sintered (cast and printed) foams prepared at different mixing intensities and, hence, relative densities are tested under compression (Instron 5566) at a displacement rate of 1 μm/s. The top and bottom surfaces of each specimen are polished to ensure a uniform load distribution. The yield strength (σ_y) is defined by the stress at which 0.2% plastic deformation occurs, while the elastic modulus (E) is defined by the slope of the stress versus strain curve between 50 and 80% σ_y.

3. RESULTS

3.1. Binary Colloidal Gel Foams. A two-step process is used to create foam-based inks for the direct writing of hierarchically porous ceramics. In the first step, a binary colloidal gel is produced by tailoring the solution pH and surfactant (decylamine) concentration to simultaneously promote the formation of a binary colloidal gel (Figure 1a) and, subsequently, drive both particle populations to attach at the liquid–air interfaces (Figure 1b) introduced via mechanical frothing. The particle attachment energy (ΔE) is given by

$$\Delta E = \pi r_p^2 \gamma_{lg} (1 - \cos\theta)^2, \qquad \theta < 90° \tag{3}$$

where r_p is the particle radius, γ_{lg} is the liquid–air interfacial energy, and θ is the contact angle (Figure 1b).[28] Since both particle populations have similar radii, their ΔE values should be comparable based on eq 3. The measured values of γ_{lg} range from 72.8 mN/m, the value for pure water,[28] to ~60 mN/m over the range of surfactant concentrations probed (Figure S1). When θ = 14–90°, the calculated particle attachment energy exceeds $10^3 k_B T$, where k_B is the Boltzmann constant and T is the absolute temperature[8,28] for both particle populations.[8,28,30,31] Stabilization of the liquid–air interface prevents bubbles entrained within binary colloidal gels from coalescing due to van der Waals forces or Ostwald ripening.[28,29,32,33] In fact, the resulting binary colloidal gel foams exhibit a stable foam microstructure in

https://dx.doi.org/10.1021/acsami.0c22292
ACS Appl. Mater. Interfaces XXXX, XXX, XXX–XXX

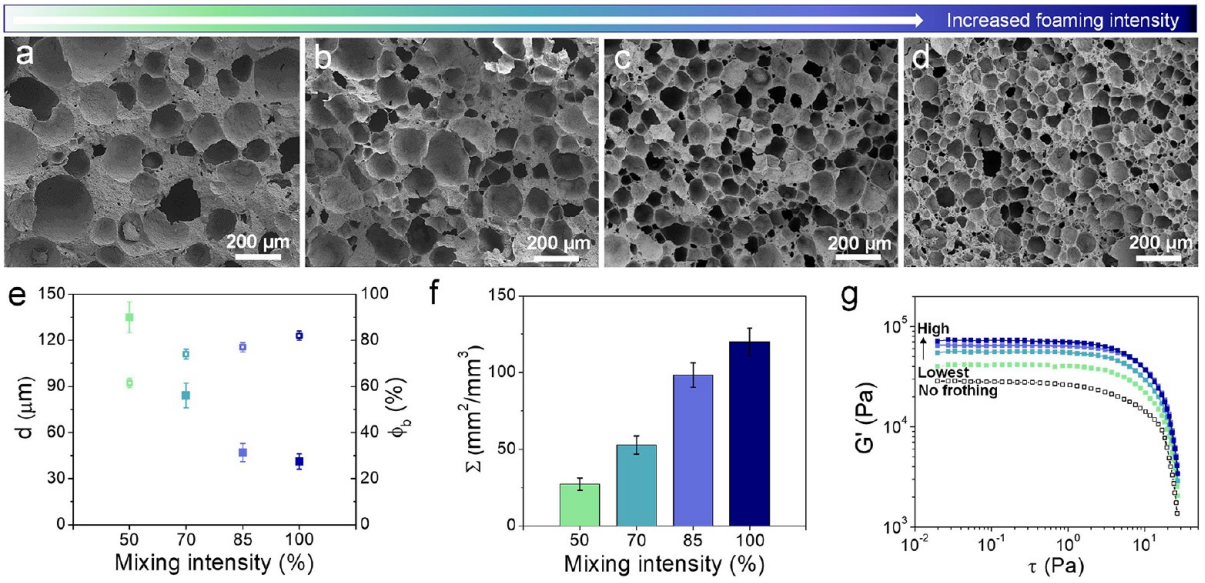

Figure 2. Mixing effects on binary colloidal gel foam microstructure and elasticity. (a–d) Micrographs of dried green foams obtained with 50, 70, 85, and 100% mixing intensity protocols, respectively. Plots for (e) average bubble size, d, bubble volume fraction, ϕ_b, and (f) specific interfacial area, Σ, vs mixing intensity. (g) Storage moduli $[G']$ as a function of shear stress $[\tau]$ for foams subjected to the different mixing protocols.

the wet state that remains unchanged during storage over periods ranging from several days to weeks. These foam-based inks enable the fabrication of hierarchically porous ceramic architectures via direct foam writing (Figure 1c). To drive the surfactant adsorption, the inks are adjusted to a pH > 10 to induce a negative charge on both alumina and carbon particles (Figure 1d). Despite their relatively high zeta potential values (−25 mV for alumina and −45 mV for carbon) under these conditions, these hydrophobically modified particles undergo gelation leading to the desired viscoelastic response for direct ink writing. For example, the binary colloidal gel and foam inks (Λ = 0.9 μmol/m^2, pH = 10.25, ϕ_c = 0.14) exhibit a strong shear-thinning behavior (Figure 1e), with apparent viscosity values ranging from ∼4 × 10^4 Pa·s at 10^{-3} s^{-1} to ∼0.07 Pa·s at 10^2 s^{-1} (gel inks) and from ∼6 × 10^4 Pa·s at 10^{-3} s^{-1} to ∼0.11 Pa·s at 10^2 s^{-1} (foam inks). Moreover, these inks also exhibit a solid-like response, that is, their storage modulus (G') exceeds their loss modulus (G''), in the linear elastic regime, with G' values of ∼3 × 10^4 Pa (gels) and ∼10^5 Pa (foams) at their corresponding shear yield stresses of τ_y ∼ 25 Pa and τ_y ∼ 100 Pa. Unless otherwise stated, the binary colloidal gels used to create foam inks in the present work are produced using the following standard conditions: Λ = 0.9 μmol/m^2, pH = 10.25, and ϕ_c = 0.14.

Controlling the foam ink microstructure is crucial to achieving hierarchically porous ceramics with open cells (mesoscale pores) surrounded by microporous cell walls. The bubble volume fraction and characteristic size are greatly influenced by the foaming intensity used during mechanical frothing (Figure 2) as well as the surfactant concentration (Figure S2). To explore the effects of mixing intensity, we created a standard binary colloidal gel with a constant alumina to carbon volume ratio of 30:70. As the foaming intensity increased from 50 to 100%, we observed pronounced microstructural changes (Figure 2a–d). Indeed, we find that the average bubble size, d, decreases from ∼135 to ∼40 μm, while the bubble volume fraction, ϕ_b, increases from ∼0.6 to ∼0.8 (Figure 2e) over these frothing conditions. During this process, the binary colloidal gel network is subjected to high shear rates that disrupt the attractive bonds between particles allowing them to adsorb onto the liquid–air interface during air entrainment. The specific interfacial area Σ increases from ∼30 to ∼120 mm^2/mm^3 as ϕ_b increases (Figure 2f), driving even more particles to the bubble walls. Once mechanical frothing ceases, the attractive particle network quickly reforms around each entrained bubble resulting in stiffer foam inks, where G' increases from ∼3 × 10^4 Pa (gel) to ∼4 × 10^4 Pa (foam, 50% mixing intensity) to ∼8 × 10^4 Pa (foam, 100% mixing intensity) (Figure 2g). Since the adsorption energy of particles at the liquid–air interface is at least 2 orders of magnitude higher than the estimated attractive interactions between particles within the (bulk) gel network (e.g., $\gtrsim 10^3 k_B T$ vs ∼$10 k_B T$), we posit that the enhanced foam ink elasticity arises from a greater connectivity between interspersed bubbles within the gel matrix. Importantly, we find that ink stiffness increases linearly with Σ (Figure S3) akin to unary colloidal foam inks reported previously.[16]

The foam ink microstructure and stiffness also depend on the composition of the binary colloidal gels mechanically frothed at a constant mixing intensity (Figure S2a–d). As one example, we changed the particle hydrophobicity by varying the surfactant concentration. For foam inks generated at 100% mixing intensity, the average bubble size decreases from ∼100 to ∼40 μm, as Λ increases from 0.3 to 0.9 μmol/m^2 (Figure S2e). However, no further reduction in characteristic bubble size is observed at higher surfactant concentrations, that is, Λ = 1.2 μmol/m^2, suggesting that the particle surfaces are already saturated. Over this same surfactant concentration range, ϕ_b increases from ∼0.67 to ∼0.84 (Figure S2e), resulting in a concomitant increase in Σ from ∼35 to ∼120 mm^2/mm^3 (Figure S2f). These microstructural changes result in an increased foam ink stiffness that ranges from G' ∼ 2 × 10^4 at Λ = 0.3 μmol/m^2 to G' ∼ 10^5 Pa at Λ = 1.2 μmol/m^2 (Figure S2g).

https://dx.doi.org/10.1021/acsami.0c22292
ACS Appl. Mater. Interfaces XXXX, XXX, XXX–XXX

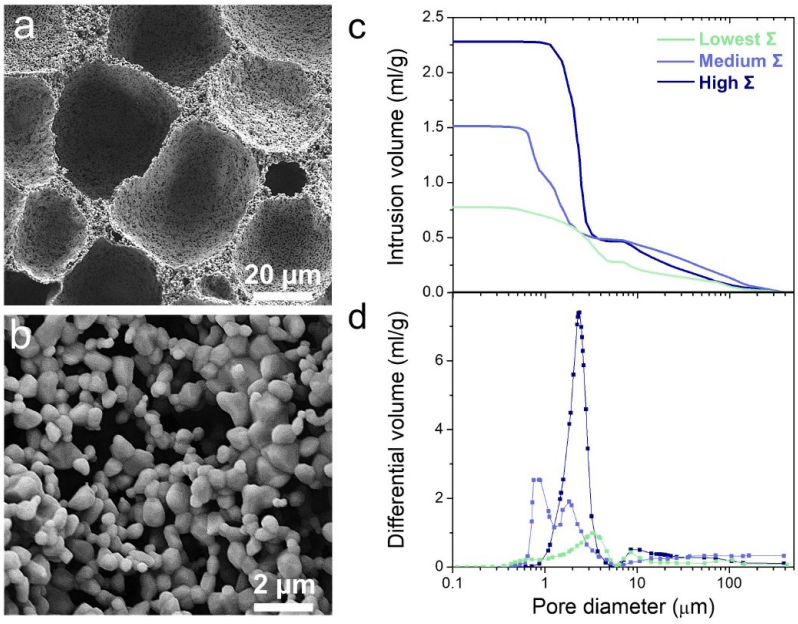

Figure 3. Hierarchically porous ceramic foams. (a) SEM image of a representative sintered ceramic foam depicting large pores arising from entrained bubbles. (b) High-magnification image of an open-cell wall surrounding the entrained bubble that arises from the removal of carbon black (porogen) particles. (c,d) Semilog plots of cumulative volume and differential volume of mercury intruded into representative sintered ceramic foams with lowest, medium, and high Σ, respectively.

Table 1. Properties of Binary Colloidal Gel Foams

Foam type	Binary colloid gel foams (cast and dried)			Hierarchically porous foams (sintered)		
	Bubble size (μm)	Bubble volume (%)	Specific interfacial area, Σ (mm^2/mm^3)	Bubble size (μm)	Total porosity (%)	Wall thickness (μm)
Lowest Σ	135	61−62	27	∼100	76	5−15
Low Σ	84	74	53	63	81	5−6
Medium Σ	47	77	98	35	86	3
High Σ	41	82	120	31	90	1−2

3.2. Microstructural Evolution and Properties of Hierarchically Porous Ceramic Foams. Sintered ceramic foams possess an open, hierarchically porous microstructure (Figure 3). Scanning electron microscopy (SEM) images reveal large pores (10's μm in diameter) corresponding to entrained bubbles, which are surrounded by fine porous walls with a characteristic thickness of ∼1 μm. These representative ceramic foams (produced at 100% mixing intensity) undergo ∼23% linear shrinkage during sintering, leading to a reduction in their average bubble size from ∼40 μm (as-cast and dried) to ∼31 μm (sintered) (Figure 3a), as summarized in Table 1. Microporous cell walls are achieved using an alumina/carbon particle ratio of 30:70 by volume (Figures S4 and 3b). To further assess their porosity, we carried out mercury intrusion porosimetry measurements on three representative sintered ceramic foams prepared at 50% (lowest Σ), 85% (medium Σ), and 100% (high Σ) mixing intensities corresponding to relative densities, ρ_{rel}, of ∼24, ∼14, and ∼10%, respectively (Figure 3c). These data reveal that the mesoscale pores, associated with entrained air bubbles, range in diameter from ∼10 to 150 μm, while micropores within the open-cell walls range in size from ∼0.3 to ∼4 μm in diameter (Figure 3d). These fine pores arise when either individual carbon (porogen) particles or clusters volatilize when heated in an oxidative environment during the sintering process.

Next, we explored the effects of hierarchical foam porosity on their fluid transport and filtration properties. Representative sintered ceramic foams with relative densities of ρ_{rel} ∼ 10% (high Σ), ρ_{rel} ∼ 14% (medium Σ), and ρ_{rel} ∼ 19% (low Σ) are prepared from standard binary colloidal gels mechanically frothed at different mixing intensities. We measured the normalized pressure drop $\Delta P/L$ across each foam sample as a function of gas velocity (Figure 4a) and used eq 2 to calculate their permeability (Figure 4b). Their estimated k values lie within a relatively narrow range, decreasing from 9×10^{-13} to 2×10^{-13} m^2 with increasing relative density. This observation likely reflects tortuosity effects that arise as the thickness of bubble walls increases. Since their measured permeability is akin to values reported for commercial diesel particulate filters,[2,27,34] we explored their ability to filter fluorescent PS particles representative of diesel exhaust (∼1 μm in diameter) (Figure 4c). Confocal microscopy reveals that a thin, relatively dense layer of PS particles accumulates onto the foam surface. The corresponding cross-sectional images of these foams shows that >99% of the PS particles are trapped within the first 100 μm of these structures. We note that their filtration efficiency may be further enhanced due to electrostatic attractions between the oppositely charged particles and the ceramic foam.

To determine their mechanical properties, we carried out compression tests on several sintered ceramic foams with

https://dx.doi.org/10.1021/acsami.0c22292
ACS Appl. Mater. Interfaces XXXX, XXX, XXX−XXX

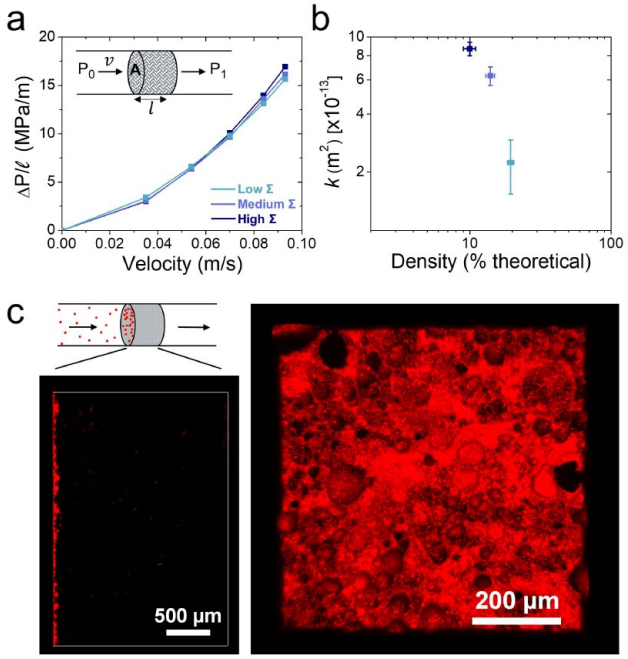

Figure 4. Permeability and filtration ability of open-cell foams. (a) Normalized pressure-drop values as a function of the velocity of an air jet for standard open-cell specimens with low, medium, and high values for Σ. In the inset, diagram of the experimental setup of pressure drop tests carried out with an air flow. (b) Permeability of the specimens as a function of sintered ceramic foam density. (c) Confocal microscopy cross-section and surface images of an open-cell foam after a filtration test with 1 μm fluorescent latex beads showing no penetration after the third layer of bubbles.

different Σ values. These foams are prepared from standard binary colloidal gels frothed at different mixing intensities. The sintered ceramic foams, which have ρ_{rel} ranging from 7 to 25%, exhibit similar microstructural features (Figure 5a) as their presintered counterparts (Figure 2a–d). The stress–strain curves for open-cell foams subjected to compressive loading are shown in Figure 5b. During initial loading, they exhibit a linear deformation attributable to elastic bending of the cell walls that surround the larger pores.[1] This behavior persists up to ∼4% strain for foams with the lowest Σ values. Their Young's modulus (E) is plotted as a function of the foam density in Figure 5c, which decreases from $E \sim 400$ MPa to $E \sim 13$ MPa as ρ_{rel} decreases from ∼25 to ∼7%. Fitting these data using eq 4, we find a power law exponent, n of ∼2.3, which exceeds the expected value of $n \sim 2$ for open-cell foams.[1]

$$\frac{E}{E_0} = \left(\frac{\rho}{\rho_{th}}\right)^n \tag{4}$$

Above their plateau stress (σ_y), each foam exhibits a nearly flat stress–strain curve that likely reflects the sequential brittle fracture of open-cell walls in a layerwise manner under compression.[1] The measured values range from $\sigma_y = 0.7$ MPa for high Σ foams ($\rho_{rel} \sim 7\%$) to $\sigma_y = 19$ MPa for the lowest Σ foams ($\rho_{rel} \sim 25\%$), as shown in Figure 5d. Fitting these data using eq 5, with $\sigma_{y,o}$ as the theoretical yield strength for dense alumina, we find a power law exponent of $n = 2.6$ that again exceeds the value expected for most open-cell foams[1]

$$\frac{\sigma_y}{\sigma_{y,0}} = \left(\frac{\rho}{\rho_{th}}\right)^n \tag{5}$$

We posit that this discrepancy arises due to the hierarchically porous nature of our ceramic foams, which consist of discrete mesoscale bubbles surrounded by microporous cell walls. By contrast, conventional (reticulated) ceramic foams contain mesoscale pores that are interconnected via open windows between adjacent cells and surrounded by dense slender beams.[1] Further study of this new class of hierarchical ceramic foams is needed to fully understand their observed scaling behavior.

3.3. Direct Writing of 3D Ceramic Foam Lattices. To introduce controlled porosity at the macroscale, we printed foam-based inks through a fine nozzle (610 μm in diameter) at a speed of 37 mm/s to produce 3D ceramic foam lattices (Figure 6a–d). The printed lattices consist of a simple cubic (or tetragonal) geometry with 20 printed layers, overall dimensions of 18 mm × 18 mm × 12 mm and a center-to-center spacing of ∼2 mm between adjacent struts. During sintering, they exhibit an isotropic, linear shrinkage of ∼23% and retain their hierarchical open-cell morphology. Akin to their bulk (cast) counterparts, the 3D lattice struts contain mesoscale pores that arise from entrained bubbles surrounded by microporous cell walls that are generated upon the removal of carbon black porogen particles during sintering. Additionally, these 3D lattices contain an 8 × 8 array of interconnected macroscale porous features that reside between printed struts. We established a printing window for direct writing of these binary colloidal gel foam inks by exploring a range of nozzle diameters (330–840 μm) and print speeds (5–200 mm/s), as shown in Figure 6e. While these foam-based inks exhibit clogging in the finest nozzles tested, they flow readily through larger nozzles. At the lowest print speed, the inks dried too quickly to ensure high fidelity printing, while printing at the highest speed led to slightly discontinuous features.

Last, we measured the yield strength of sintered ceramic foam lattices of varying total porosity and Σ values (Figure 6f) under compression along the z-axis, which is orthogonal to the printed struts that are orthogonally patterned in a layerwise manner in the x–y plane. Due to their hierarchical porosity across three length scales, these 3D ceramic lattices possess low relative densities ranging from roughly 3 to 6% ρ_{th}. Akin to the sintered (cast) ceramic foams described above, the yield strength of these printed ceramic foams exhibits a power law dependence on relative density, where $n \sim 2.5$. We also find that these 3D foam lattices exhibit higher compressive strength values, for example, $\sigma_y \sim 2$ MPa at $\rho_{th} \sim 5.5\%$ compared to bulk (cast) foams, which must have twofold higher density ($\rho_{th} \sim 11\%$) to achieve a comparable $\sigma_y \sim 2$ MPa. Hence, by programming their open porosity across multiple length scales from the foam struts that contain mesoscale open cells surrounded by microporous walls to their 3D lattice geometry, we can tailor their permeability and mechanical properties for targeted applications of interest.

4. CONCLUSIONS

We have designed and assembled bulk and 3D printed ceramic foams with hierarchical open porosity tailored across multiple length scales. By creating binary colloidal gels that

https://dx.doi.org/10.1021/acsami.0c22292
ACS Appl. Mater. Interfaces XXXX, XXX, XXX–XXX

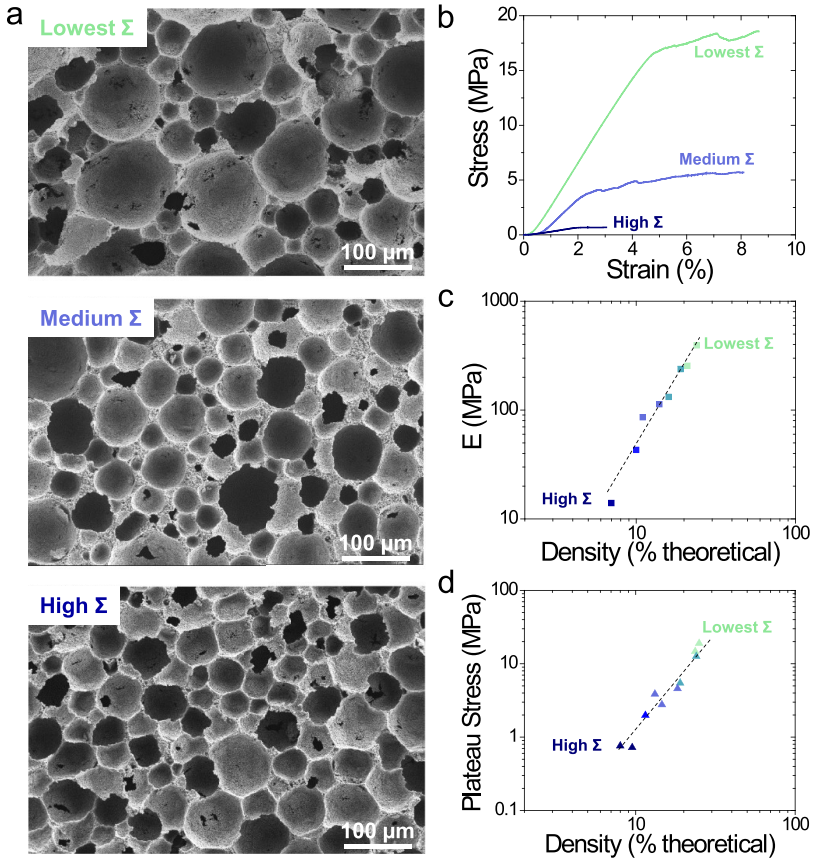

Figure 5. Mechanical behavior of hierarchically porous ceramic foams. (a) SEM images of representative sintered ceramic foams with low, medium, and high Σ values. (b) Stress–strain plots for representative sintered ceramic foams with lowest , medium, and high Σ values. (c,d) Log–log plots of the Young's modulus (E) and yield strength (σ_y) as a function of sintered ceramic foam density for representative samples of varying Σ values, both showing a power dependence with density depicted as a dotted line.

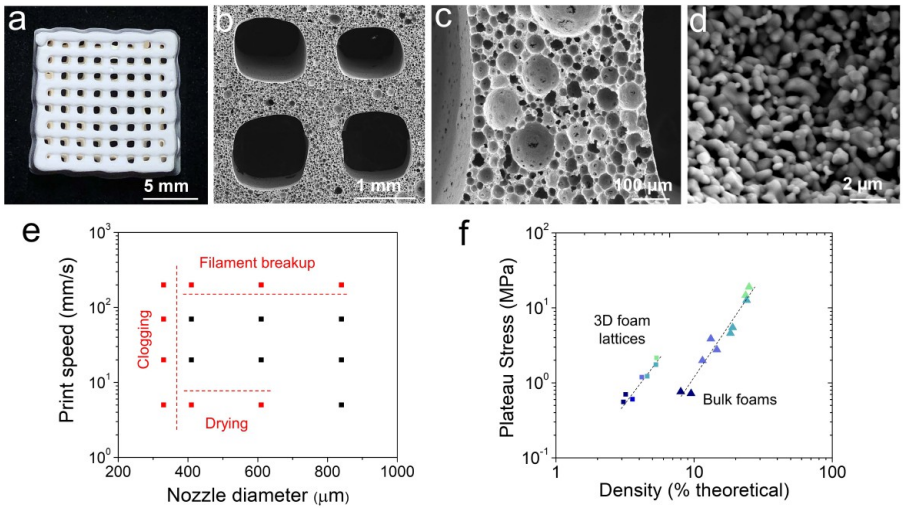

Figure 6. Direct foam writing of hierarchically porous ceramic architectures. (a) Optical image of representative printed and sintered hierarchical ceramic foam lattice. (b) SEM image of the cross-section of a printed and sintered hierarchical ceramic foam lattice showing large pore channels between printed foam struts. (c) Higher magnification SEM image of entrained bubbles within a strut in the printed and sintered hierarchical ceramic foam lattice. (d) Microstructure of a representative bubble wall. (e) Processing window for 3D printing of binary colloidal gel foams. [Note: black data points reside in the printing region]. (f) Log–log plot of yield strength as a function of sintered hierarchical ceramic foam density for printed and cast (bulk) foams of varying Σ values measured under compression along the z-axis (out-of-plane direction in Figure 6a).

contain hydrophobically modified ceramic and porogen particles, we produced foam-based inks in which both particle populations adsorb at the liquid–air interfaces of entrained bubbles generated via mechanical frothing. We showed that the characteristic bubble size and volume fraction depended on both the binary colloidal gel composition and the mixing

https://dx.doi.org/10.1021/acsami.0c22292
ACS Appl. Mater. Interfaces XXXX, XXX, XXX–XXX

intensity used during mechanical frothing. We further showed that the incorporation of carbon black porogen particles that are removed during sintering in an oxidative environment leads to open-cell walls that surround the entrained bubbles. Using direct foam writing, we printed 3D ceramic foam lattices that exhibit enhanced permeability and mechanical properties compared to bulk foams of similar relative density. Our integrated design and fabrication platform may open new avenues to creating programmable ceramic foams for myriad applications, including particle filtration, catalyst supports, and novel electrodes for flow batteries.

■ ASSOCIATED CONTENT

Supporting Information

The Supporting Information is available free of charge at https://pubs.acs.org/doi/10.1021/acsami.0c22292.

Surface tension of supernatant solutions obtained from binary colloidal gel foams with varying surfactant concentration, effects of surfactant concentration on the foam microstructure and elasticity, shear elastic modulus as a function of specific interfacial area (Σ) for binary colloidal gel foams, and distribution of alumina and carbon (porogen) particles in the cell walls within these ceramic foams (PDF)

■ AUTHOR INFORMATION

Corresponding Author

Jennifer A. Lewis − *School of Engineering and Applied Sciences, Harvard University, Cambridge, Massachusetts 02138, United States;* orcid.org/0000-0002-0280-2774; Email: jalewis@seas.harvard.edu

Authors

Benito Román-Manso − *School of Engineering and Applied Sciences, Harvard University, Cambridge, Massachusetts 02138, United States*

Joseph Muth − *School of Engineering and Applied Sciences, Harvard University, Cambridge, Massachusetts 02138, United States*

Lorna J. Gibson − *Materials Science and Engineering Department, MIT, Cambridge, Massachusetts 02139, United States*

Wolfgang Ruettinger − *BASF Corp., Iselin, New Jersey 08830, United States*

Complete contact information is available at: https://pubs.acs.org/10.1021/acsami.0c22292

Author Contributions

B.R.-M., J.M., W.R., and J.A.L. designed the research. B.R.-M. carried out the research. All authors contributed toward analyzing the data and writing the manuscript.

Funding

The authors gratefully acknowledge the funding provided by BASF and DOE BES (award #DE-SC0020170). We also thank the Harvard's Center for Nanoscale Systems (CNS) for use of their microscopy facility.

Notes

The authors declare the following competing financial interest(s): J.A.L. is the co-founder of Voxel8, Inc., which focuses on multi-material 3D printing. B.R.-M., J.M., W.R., and J.A.L. have filed a patent on this work.

■ REFERENCES

(1) Gibson, L. J.; Ashby, M. F. *Cellular Solids: Structure and Properties*; Cambridge University Press: Cambridge, 2009.

(2) *Cellular Ceramics: Structure, Manufacturing, Properties and Applications*; Scheffler, M., Colombo, P., Eds.; John Wiley & Sons: Hoboken, N.J., 2006.

(3) Gibson, L. J.; Ashby, M. F.; Harley, B. A. *Cellular Materials in Nature and Medicine*; Cambridge University Press: Cambridge, U.K., 2010.

(4) Wegst, U. G. K.; Bai, H.; Saiz, E.; Tomsia, A. P.; Ritchie, R. O. Bioinspired Structural Materials. *Nat. Mater.* **2015**, *14*, 23−36.

(5) Meyers, M. A.; McKittrick, J.; Chen, P.-Y. Structural Biological Materials: Critical Mechanics-Materials Connections. *Science* **2013**, *339*, 773−779.

(6) Fratzl, P.; Weinkamer, R. Nature's Hierarchical Materials. *Prog. Mater. Sci.* **2007**, *52*, 1263−1334.

(7) Weinkamer, R.; Fratzl, P. Solving Conflicting Functional Requirements by Hierarchical Structuring—Examples from Biological Materials. *MRS Bull.* **2016**, *41*, 667−671.

(8) Studart, A. R.; Gonzenbach, U. T.; Tervoort, E.; Gauckler, L. J. Processing Routes to Macroporous Ceramics: a Review. *J. Am. Ceram. Soc.* **2006**, *89*, 1771−1789.

(9) Gonzenbach, U. T.; Studart, A. R.; Tervoort, E.; Gauckler, L. J. Ultrastable Particle-Stabilized Foams. *Angew. Chem., Int. Ed.* **2006**, *45*, 3526−3530.

(10) Gonzenbach, U. T.; Studart, A. R.; Tervoort, E.; Gauckler, L. J. Stabilization of Foams with Inorganic Colloidal Particles. *Langmuir* **2006**, *22*, 10983−10988.

(11) Zheng, X.; Lee, H.; Weisgraber, T. H.; Shusteff, M.; DeOtte, J.; Duoss, E. B.; Kuntz, J. D.; Biener, M. M.; Ge, Q.; Jackson, J. A.; Kucheyev, S. O.; Fang, N. X.; Spadaccini, C. M. Ultralight, Ultrastiff Mechanical Metamaterials. *Science* **2014**, *344*, 1373−1377.

(12) Schaedler, T. A.; Jacobsen, A. J.; Torrents, A.; Sorensen, A. E.; Lian, J.; Greer, J. R.; Valdevit, L.; Carter, W. B. Ultralight Metallic Microlattices. *Science* **2011**, *334*, 962−965.

(13) Muth, J. T.; Dixon, P. G.; Woish, L.; Gibson, L. J.; Lewis, J. A. Architected Cellular Ceramics with Tailored Stiffness via Direct Foam Writing. *Proc. Natl. Acad. Sci. U.S.A* **2017**, *114*, 1832−1837.

(14) Deville, S. Freeze-Casting of Porous Ceramics: A Review of Current Achievements and Issues. *Adv. Eng. Mater.* **2008**, *10*, 155−169.

(15) Chuanuwatanakul, C.; Tallon, C.; Dunstan, D. E.; Franks, G. V. Producing Large Complex-Shaped Ceramic Particle Stabilized Foams. *J. Am. Ceram. Soc.* **2013**, *96*, 1407−1413.

(16) Muth, J. T.; Lewis, J. A. Microstructure and Elastic Properties of Colloidal Gel Foams. *Langmuir* **2017**, *33*, 6869−6877.

(17) Zheng, X.; Smith, W.; Jackson, J.; Moran, B.; Cui, H.; Chen, D.; Ye, J.; Fang, N.; Rodriguez, N.; Weisgraber, T.; Spadaccini, C. M. Multiscale Metallic Metamaterials. *Nat. Mater.* **2016**, *15*, 1100−1106.

(18) Meza, L. R.; Zelhofer, A. J.; Clarke, N.; Mateos, A. J.; Kochmann, D. M.; Greer, J. R. Resilient 3D Hierarchical Architected Metamaterials. *Proc. Natl. Acad. Sci. U.S.A* **2015**, *112*, 11502−11507.

(19) Meza, L. R.; Das, S.; Greer, J. R. Strong, Lightweight, and Recoverable Three-Dimensional Ceramic Nanolattices. *Science* **2014**, *345*, 1322−1326.

(20) Bauer, J.; Hengsbach, S.; Tesari, I.; Schwaiger, R.; Kraft, O. High-Strength Cellular Ceramic Composites with 3D Microarchitecture. *Proc. Natl. Acad. Sci. U.S.A* **2014**, *111*, 2453−2458.

(21) Eckel, Z. C.; Zhou, C.; Martin, J. H.; Jacobsen, A. J.; Carter, W. B.; Schaedler, T. A. Additive Manufacturing of Polymer-Derived Ceramics. *Science* **2016**, *351*, 58−62.

(22) Hammel, E. C.; Ighodaro, O. L.-R.; Okoli, O. I. Processing and Properties of Advanced Porous Ceramics: An Application-based Review. *Ceram. Int.* **2014**, *40*, 15351−15370.

(23) Meille, V. Review on Methods to Deposit Catalysts on Structured Surfaces. *Appl. Catal., A* **2006**, *315*, 1−17.

(24) Sun, K.; Wei, T.-S.; Ahn, B. Y.; Seo, J. Y.; Dillon, S. J.; Lewis, J. A. 3D Printing of Interdigitated Li-Ion Microbattery Architectures. *Adv. Mater.* **2013**, *25*, 4539−4543.
(25) Rolison, D. R.; Long, J. W.; Lytle, J. C.; Fischer, A. E.; Rhodes, C. P.; McEvoy, T. M.; Bourg, M. E.; Lubers, A. M. Multifunctional 3D Nanoarchitectures for Energy Storage and Conversion. *Chem. Soc. Rev.* **2009**, *38*, 226−252.
(26) Zhang, H.; Yu, X.; Braun, P. V. Three-Dimensional Bicontinuous Ultrafast-Charge-and-Discharge Bulk Battery Electrodes. *Nat. Nanotechnol.* **2011**, *6*, 277−281.
(27) Adler, J. Ceramic Diesel Particulate Filters. *Int. J. Appl. Ceram. Technol.* **2005**, *2*, 429−439.
(28) Binks, B. P. Particles as Surfactants—Similarities and Differences. *Curr. Opin. Colloid Interface Sci.* **2002**, *7*, 21−41.
(29) Gonzenbach, U. T.; Studart, A. R.; Tervoort, E.; Gauckler, L. J. Macroporous Ceramics from Particle-Stabilized Wet Foams. *J. Am. Ceram. Soc.* **2007**, *90*, 16−22.
(30) Frelichowska, J.; Bolzinger, M.-A.; Chevalier, Y. Effects of Solid Particle Content on Properties of o/w Pickering Emulsions. *J. Colloid Interface Sci.* **2010**, *351*, 348−356.
(31) Megias-Alguacil, D.; Tervoort, E.; Cattin, C.; Gauckler, L. J. Contact Angle and Adsorption Behavior of Carboxylic Acids on α-Al2O3 Surfaces. *J. Colloid Interface Sci.* **2011**, *353*, 512−518.
(32) Aveyard, R.; Binks, B. P.; Clint, J. H. Emulsions Stabilised Solely by Colloidal Particles. *Adv. Colloid Interface Sci.* **2003**, *100−102*, 503−546.
(33) Finkle, P.; Draper, H. D.; Hildebrand, J. H. The Theory of Emulsification. *J. Am. Chem. Soc.* **1923**, *45*, 2780−2788.
(34) Konstandopoulos, A. G. Flow Resistance Descriptors for Diesel Particulate Filters: Definitions, Measurements and Testing. *SAE Technical Paper*, 2003, 2003-01-0846.

https://dx.doi.org/10.1021/acsami.0c22292
ACS Appl. Mater. Interfaces XXXX, XXX, XXX−XXX